

# Self-similar asymptotics for a class of Hele-Shaw flows driven solely by surface tension

Baruch Meerson<sup>a</sup>, Pavel V. Sasorov<sup>b</sup>, Arkady Vilenkin<sup>a</sup>

<sup>a</sup>*Racah Institute of Physics, Hebrew University of Jerusalem, Jerusalem 91904, Israel*

<sup>b</sup>*Institute of Theoretical and Experimental Physics, Moscow 117218, Russia*

---

## Abstract

We investigate the dynamics of relaxation, by surface tension, of a family of curved interfaces between an inviscid and viscous fluids in a Hele-Shaw cell. At  $t = 0$  the interface is assumed to be of the form  $|y| = Ax^m$ , where  $A > 0$ ,  $m \geq 0$ , and  $x > 0$ . The case of  $0 < m < 1$  corresponds to a smooth shape,  $m > 1$  corresponds to a cusp, whereas  $m = 1$  corresponds to a wedge. The inviscid fluid tip retreats in the process of relaxation, forming a lobe which size grows with time. Combining analytical and numerical methods we find that, for any  $m$ , the relaxation dynamics exhibit self-similar behavior. For  $m \neq 1$  this behavior arises as an intermediate asymptotics: at late times for  $0 \leq m < 1$ , and at early times for  $m > 1$ . In both cases the retreat distance and the lobe size exhibit power law behaviors in time with different dynamic exponents, uniquely determined by the value of  $m$ . In the special case of  $m = 1$  (the wedge) the similarity is exact and holds for the whole interface at all times  $t > 0$ , while the two dynamic exponents merge to become  $1/3$ . Surprisingly, when  $m \neq 1$ , the interface shape, rescaled to the local maximum elevation of the interface, turns out to be universal (that is, independent of  $m$ ) in the similarity region. Even more remarkably, the same rescaled interface shape emerges in the case of  $m = 1$  in the limit of zero wedge angle.

*Key words:* unforced Hele-Shaw flow, surface tension, relaxation, scaling, power law, self-similarity

---

## 1. Introduction

Consider a curved interface between a low-viscosity fluid (for example, water) and a high-viscosity fluid (for example, oil) in a large horizontal Hele-Shaw cell. If the system is unforced, the interface undergoes relaxation by surface tension, ultimately approaching either a straight line, or a circle (or breaking into several domains which then become circles). This free boundary problem is hard to solve, as the governing equations (see below) are non-local. This is especially true when the interface initially has a complex shape, as observed in numerous experiments when the viscous fluid is displaced by the inviscid fluid in radial geometry, see Ref. [1] and references therein. The initial shape

complexity is caused here by the viscous fingering instability that develops during the preceding *forced* stage of the flow [2,3]. The (strongly) forced Hele-Shaw flow is a standard paradigm in fluid dynamics and nonlinear dynamics [4,5,6,7]. The (small) surface tension there is usually invoked in order to regularize the otherwise singular dynamics on small scales. We are interested in this paper in an *unforced* flow, where surface tension is the *only* driving mechanism. Here is the formulation of the unforced Hele-Shaw (UHS) flow model that we will be dealing with throughout this paper. Let one fluid have negligible viscosity, so that the pressure in it is uniform. The velocity of the viscous fluid is  $\mathbf{v}(\mathbf{r}, t) = -(H^2/12\mu) \nabla p(\mathbf{r}, t)$ , where  $p$  is the pressure,  $\mu$  is the dynamic viscosity, and  $H$  is the plate spacing [2,3,4,5]. Therefore, the interface speed is

$$v_n = -(H^2/12\mu) \partial_n p, \quad (1)$$

where index  $n$  denotes the components of the vectors normal to the interface and directed from the inviscid fluid to the viscous fluid, and  $\partial_n p$  is evaluated at the corresponding point of the interface  $\gamma$ . The viscous fluid is incompressible. Therefore, its pressure is a harmonic function:

$$\nabla^2 p = 0. \quad (2)$$

The Gibbs-Thomson relation yields a boundary condition at the interface:

$$p|_\gamma = (\pi/4) \sigma \mathcal{K}, \quad (3)$$

where  $\sigma$  is surface tension, and  $\mathcal{K}$  is the local curvature of the interface, positive when the inviscid region is convex outwards. Finally, as the flow is unforced, we demand

$$\nabla p = 0 \quad \text{at} \quad \mathbf{r} \rightarrow \infty. \quad (4)$$

Equations (1)-(4) define the UHS problem (see Refs. [8,9,10] and references therein for a more detailed discussion). The UHS model gives an instructive example of non-local area-preserving curve-shortening dynamics.

The UHS flow (1)-(4) is not integrable. Moreover, until recently even no *particular* analytic solutions to this class of flows had been found, except for the simple solutions provided by a linear stability analysis of a single, slightly deformed flat or circular interface [11]. Recently, some analytic solutions have been obtained for two special initial interface shapes. In the first of them, the inviscid fluid domain at  $t = 0$  has the form of a half-infinite stripe [12]. As time progresses, the tip of the stripe retreats and develops a lobe. At long times, the growing lobe approaches a self-similar shape, whereas the lobe size and retreat distance follow a power law in time with different dynamic exponents:  $1/5$  and  $3/5$ , respectively.

In the second case the assumed form of the inviscid fluid was a wedge [13]. As this initial condition, and Eqs. (1)-(4), do not introduce any length scale into the problem, the solution is self-similar at *all* times, with a single dynamic exponent  $1/3$  [13]. The scale-invariant interface shape in this case is given by the solution of an unusual inverse problem of potential theory. Gat *et al.* [13] solved this problem perturbatively for an almost flat wedge, and numerically for several values of the wedge angle.

The results of Refs. [12,13] suggest that the values of dynamic exponents, and other attributes of the

self-similar asymptotics, are determined by the initial shape of the retreating edge of the inviscid fluid domain, while the two solutions obtained in Refs. [12,13] are particular members of a broader family of solutions. The results of the present paper confirm this scenario. We consider here a more general, power-law shape  $|y| = Ax^m$ , where  $A > 0$ ,  $m \geq 0$ , and  $x > 0$ , and show that, for *any*  $m \geq 0$ , the relaxation dynamics exhibit self-similar intermediate asymptotics: a late-time asymptotics for  $0 \leq m < 1$  and an early-time asymptotics for  $m > 1$ . The retreat distance and the lobe size show, for any  $m$ , a power law behavior in time with exponents and pre-factors uniquely determined by  $m$ . The case of  $m = 1$ , investigated in Ref. [13], is special: here the self-similarity is exact and occurs for *all* times  $t > 0$ , while the two dynamic exponents merge and become equal to  $1/3$ . Surprisingly, at  $m \neq 1$  the interface shape, rescaled to the local maximum elevation of the interface, turns out to be universal (that is, independent of  $m$ ) in the similarity region. Even more remarkably, the same rescaled interface shape emerges in the case of  $m = 1$  in the limit of zero wedge angle.

Here is a layout of the rest of the paper. In Section II we generalize to an arbitrary  $m \geq 0$  the approach, suggested by Vilenkin *et al.* [12] for a half-infinite stripe ( $m = 0$ ). We present there a simple asymptotic scaling analysis that predicts (i) the dynamic exponents of the self-similar part of the flow, (ii) the exponent of the power-law tail of the scale-invariant shape function of the interface, and (iii) the validity range of the scaling behavior at  $0 \leq m < 1$  and  $m > 1$ . In Section III we report the results of a numerical solution of (1)-(4) for the cases of  $m = 1/4$ ,  $1/2$  and  $5/4$ , compare them with our theoretical predictions and report the universality of the rescaled interface shape. In addition, we present in Section III our new numerical results for small-angle wedges. A brief discussion and summary are presented in Section IV.

## 2. Interface dynamics: theoretical predictions

Let at  $t = 0$  the interface shape be  $|y| = Ax^m$ , where  $A > 0$ ,  $m \geq 0$ , and  $x > 0$ . The case of  $0 < m < 1$  corresponds to smooth shapes,  $m > 1$  corresponds to a cusp, see Fig. 1, while  $m = 1$  corresponds to a wedge. The parameter  $A$  has the dimension of  $length^{1-m}$ . This implies that the case of  $m = 1$ , investigated by Gat *et al.* [13], is special,

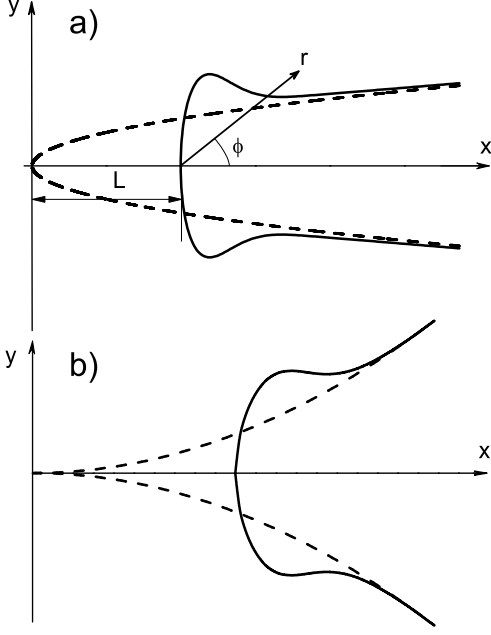


Fig. 1. A schematic setting for the interface dynamics for  $0 \leq m < 1$  (a) and  $m > 1$  (b).

as the parameter  $A$  does not introduce any length scale there. We assume in this Section that  $m \neq 1$  and measure the distance in units of  $\Delta \equiv A^{1/(1-m)}$ , the time in units of  $\tau = 48\mu\Delta^3/(\pi\sigma H^2)$ , and the pressure in units of  $p_0 = \pi\sigma/(4\Delta)$ . In the rescaled variables the interface shape is  $|y| = x^m$ , while Eqs. (1) and (3) are parameter-free:

$$v_n = -\partial_n p \quad (5)$$

and

$$p|_\gamma = \mathcal{K}. \quad (6)$$

Because of the finite surface tension, the pressure gradient in the viscous fluid is largest at the tip, so the tip will retreat along the x-axis and develop a lobe which size will grow with time. Let us assume (and then test numerically) that the evolving interface can be fully characterized by *two* time-dependent length scales: the curvature radius,  $R(t)$ , and the retreat distance,  $L(t)$ , of the tip. In the leading order this assumption implies a similarity ansatz, in the moving frame  $x_1 = x - L(t)$ , for the interface elevation  $y = h(x, t)$  in the lobe region and region II (see below):

$$h_s(x_1, t) = R(t) \Phi \left[ \frac{x_1}{R(t)} \right]. \quad (7)$$

In the scaling regime, the dynamic length scales  $L(t)$  and  $R(t)$  exhibit a power law behavior:

$$L(t) = a t^\alpha \quad \text{and} \quad R(t) = b t^\beta, \quad (8)$$

where the exponents  $\alpha$  and  $\beta$  and coefficients  $a$  and  $b$  are  $m$ -dependent. The objectives of this work is to determine analytically  $\alpha$ ,  $\beta$  the exponent of the power-law tail of the scale-invariant shape function of the interface  $\Phi[x_1/R(t)]$ , and the validity range of the scaling behavior at  $0 \leq m < 1$  and  $m > 1$ . These analytic findings will be verified and complemented by our numerical solutions which, in addition, provide the whole scale-invariant shape function  $\Phi[x_1/R(t)]$  and the coefficients  $a$  and  $b$  of the power laws of  $R(t)$  and  $L(t)$  for four different values of  $m$ , in Sec. III.

A simple asymptotic scaling analysis for  $m \neq 1$  is possible because of the following property of the initial shape of the inviscid fluid region: it has a flat region at either very large distances  $x \gg 1$  (for  $0 \leq m < 1$ ), or very small distances  $x \ll 1$  (for  $m > 1$ ). We will see that, as a result, the scaling regime will hold at  $t \gg 1$  for  $0 \leq m < 1$  and at  $t \ll 1$  for  $m > 1$ . The calculations are very similar to those of Ref. [12], where the particular case of  $m = 0$  was considered. Introduce for a moment the system of polar coordinates  $r$  and  $\phi$  with the origin at the moving tip of the interface, as shown in Fig. 1a. In view of the Gibbs-Thomson condition (6),  $p$  must vanish, in the leading order, at the flat region, that is at  $\phi \rightarrow 0$  and  $\phi \rightarrow 2\pi$ . This corresponds either to the region  $1 \ll R(t) \ll r$  for  $0 \leq m < 1$ , or to the region  $R(t) \ll r \ll 1$  for  $m > 1$ . Furthermore, in view of the same Eq. (6),  $p = \mathcal{K} \sim 1/R(t)$  in the lobe region (for definiteness, at  $\phi = \pm\pi/2$ ). Therefore, the leading term of the far-field multipole expansion of  $p$  [14] can be written as

$$p(r, \phi, t) = C_m [R(t) r]^{-1/2} \sin(\phi/2), \quad (9)$$

where  $C_m = \mathcal{O}(1)$ . Having demanded the boundary condition (6) in Eq. (9), we stretched the validity region of Eq. (9),  $r \gg R(t)$ , toward  $r \sim R(t)$ , but this can only affect the value of constant  $C_m$  that our theory cannot give anyway. Now we can employ Eqs. (5) and (9) and estimate the normal component of the interface speed in the far field region. For the upper interface of the far field region

$$v_n = -\frac{1}{r} \frac{\partial p}{\partial \phi}(\phi \rightarrow 0) = -\frac{C_m}{2R^{1/2}(t) r^{3/2}}. \quad (10)$$

At this point we return to the Cartesian coordinates  $x_1, y$ . In the far field region, that is at  $1 \ll R(t) \ll$

$x_1$  for  $0 \leq m < 1$  or  $R(t) \ll x_1 \ll 1$  for  $m > 1$ , the quantity  $\partial h(x_1, t)/\partial t$  is given by Eq. (10), and we obtain

$$h(x_1, t) - x^m = \int_0^t \frac{C_m dt'}{2R^{1/2}(t')x_1^{3/2}}. \quad (11)$$

As we will check *a posteriori*,  $L(t)$  is always much greater than  $R(t)$  in the scaling regime. How can we simplify the calculation of the integral in Eq. (11)? The far field region  $x_1 \gg R(t)$  can be divided into two sub-regions:  $x_1 \gg L(t)$  (region I) and  $R(t) \ll x_1 \ll L(t)$  (region II, or neck). In region I we can, in the leading order, take  $x_1^{3/2}$  out of the integral and arrive at

$$h(x_1, t) - x^m \simeq \frac{C_m}{2x_1^{3/2}} \int_0^t \frac{dt'}{R^{1/2}(t')} \sim \frac{t}{x_1^{3/2} R^{1/2}(t)}, \quad (12)$$

where we have assumed that  $R(t)$  is a power of  $t$ , and disregarded the coefficient  $C_m = \mathcal{O}(1)$ .

In region II at fixed  $x$ , the main contribution to the integral in Eq. (11) comes from times close to  $t$ , so that  $x_1(t)/\dot{L}(t) \ll t - t' \ll t$ . Indeed, we can expand  $x_1(t') = x_1(t) + \dot{L}(t)(t - t') + \dots$  and, in the leading order, neglect higher order terms. The effective time interval for the integration is  $(t - \delta t', t)$ , where  $\delta t' \sim x_1(t)/\dot{L}(t)$ . Furthermore,  $R^{1/2}(t')$  can be evaluated at  $t' = t$ , as its variation on the time interval  $(t - \delta t', t)$  is negligible. Then, extending the lower limit of the integral to  $-\infty$  and calculating the remaining elementary integral, we obtain

$$h(x_1, t) - x^m \sim \frac{C_m}{R^{1/2}(t) \dot{L}(t) x_1^{1/2}}, \quad (13)$$

where the factor  $C_m = \mathcal{O}(1)$  is in excess of accuracy and can be disregarded. Now we can estimate the contributions of regions I and II to the area gain  $\delta A$  in the far field region. In region I (correspondingly, II) the main contribution to the integral over  $x_1$  comes from the lower (correspondingly, upper) limit of integration. Therefore, we integrate Eq. (12) over  $x_1$  from, say,  $2L(t)$  to infinity, and Eq. (13) from  $R(t)$  to  $2L(t)$ . The results are:

$$\delta A_I(t) \sim \frac{t}{L^{1/2}(t) R^{1/2}(t)} \quad \text{in region I}, \quad (14)$$

and

$$\delta A_{II}(t) \sim \frac{L^{1/2}(t)}{\dot{L}(t) R^{1/2}(t)} \quad \text{in region II}. \quad (15)$$

As, by assumption,  $L(t)$  is a power law,  $\delta A_I$  is comparable to  $\delta A_{II}$ . As we will check shortly, the contribution to the area of the lobe region itself,  $\delta A_R \sim R^2(t)$ , is negligible compared to  $\delta A_I$  and  $\delta A_{II}$  as long as we are in the scaling regime ( $t \gg 1$  for  $0 \leq m < 1$  or  $t \ll 1$  for  $m > 1$ ).

Now we employ the exact integral of motion of the system: the area conservation of each of the fluids. The area loss because of the retreat [which is equal to  $L(t)^{m+1}/(m+1) \sim L(t)^{m+1}$ ] must be equal, in the leading order, to the area gain in the far field region. This follows

$$L(t)^{m+1} \sim \delta A_I(t) \sim \delta A_{II}(t),$$

which yields a relation between the two dynamic length scales  $R(t)$  and  $L(t)$ . Another relation between these two quantities follows from Eq. (9). We obtain  $V_l \sim -\partial p/\partial r [r \sim R(t), \phi \simeq \pi] \sim R^{-2}(t)$ , and demand

$$\dot{L}(t) \sim R^{-2}(t).$$

These two relations immediately yield the dynamic exponents  $\alpha$  and  $\beta$ :

$$\alpha = \frac{3}{4m+5} \quad \text{and} \quad \beta = \frac{2m+1}{4m+5}. \quad (16)$$

Once the scaling relations for  $L(t)$  and  $R(t)$  are found, we can calculate [up to  $m$ -dependent numerical pre-factors  $\mathcal{O}(1)$ ], additional quantities. For example, the interface elevation in region I becomes

$$h(x, t) - x^m \sim t^{\frac{3(2m+3)}{2(4m+5)}} x^{-3/2},$$

see Eq. (12). In region II, see Eq. (13), we obtain

$$h(x, t) - x^m \sim t^{\frac{3(2m+1)}{2(4m+5)}} x^{-1/2}.$$

Importantly, region II belongs to the similarity region, as was first observed in Ref. [12] in the case of  $m = 0$ . In this region  $\Phi(\xi) \sim \xi^{-1/2}$ : a universal ( $m$ -independent) power law of the similarity variable  $\xi = x_1/R(t)$ . The presence of the decreasing asymptote  $\Phi(\xi) \sim \xi^{-1/2}$  implies that, for any  $m \neq 1$ , the shape function  $\Phi(\xi)$  must have a local maximum.

Once we obtained the solution, we can check it for self-consistency with all the assumptions we made. First, it can be easily checked that, in the scaling regime  $t \gg 1$  (for  $0 \leq m < 1$ ) or  $t \ll 1$  (for  $m > 1$ ) we have  $L(t) \gg R(t)$ , as we assumed. Now, the lobe area  $\delta A_R \sim R^2(t)$  grows with time as  $\sim t^{2(2m+1)/(4m+5)}$ . This value is indeed much less than  $\delta A_I(t) \sim \delta A_{II}(t) \sim t^{3(m+1)/(4m+5)}$  in the scaling regime. Furthermore, the time-dependent interface elevation in the lobe region  $R(t) \sim L(t)^{(2m+1)/3}$  is

much larger, in the scaling regime, than the initial interface elevation at the moving tip, which is  $L(t)^m$ . This strong inequality serves as a necessary condition for the assumed similarity asymptotics (7) as a leading order description.

### 3. Numerical solution

In order to test the predicted dynamic exponents  $\alpha$  and  $\beta$  and verify the presence of the self-similar regime, we solved the problem numerically for three different values of parameter  $m$ . In addition, we returned to the case of  $m = 1$ , previously considered in Ref. [13], and solved it numerically for small values of the wedge angle.

#### 3.1. Numerical method

Our numerical algorithm [16] employs a variant of the boundary integral method for an exterior Dirichlet problem formulated for a singly connected domain, and explicit tracking of the contour nodes. The harmonic potential is represented as a potential produced by a dipole distribution with an *a priori* unknown density  $\mathbf{D}$  on the contour. The dipole density  $\mathbf{D}$  is found numerically from an integral equation which is a modification of the well-known jump relation of the potential theory [17]. Computing another integral of this (already found) dipole density, one obtains the harmonic conjugate function, whose derivative along the contour yields, by virtue of the Cauchy theorem, the normal velocity of the interface.

We used a piecewise constant function for a discrete approximation of  $\mathbf{D}$  and a piecewise linear function for discretizing the interface. The integral entering the integral equation is represented as a sum of  $\mathbf{D}$  multiplied by a kernel which is integrated analytically between two neighboring nodes. This approximation was previously suggested for the inner problem [15]. We found that it is also efficient in the outer problem in the following cases: (i) for a long and slender domain, (ii) in the vicinity of the cusp at  $m > 1$ , and (iii) for a wedge ( $m = 1$ ) with a small angle. The numerical approximation is described in detail in Ref. [16]. The method requires an inhomogeneous grid with a small spacing in regions of high curvature of the contour, and we used a grid with spacing exponentially growing with the distance from the interface's tip. The number of grid nodes was reduced as the interface's perimeter

decreased, and the curvature radius of the tip increased.

The shape of the numerical interface at  $t = 0$  is determined by the following parameters: the exponent  $m$ , the domain size  $\Lambda > 0$ , and the cutoff parameter  $\varepsilon > 0$  that was used for  $m \geq 1$ , see below. One quarter of the interface is represented as a graph  $h(x) = (x + \Lambda)^m$ , where  $-\Lambda + \varepsilon \leq x \leq 0$ . The second quarter is obtained by reflecting this graph with respect to the  $x$ -axis. Then, by reflecting the two branches with respect to the  $y$ -axis, we obtained the closed interface we worked with. In this manner we could exploit the four-fold symmetry of the domains and achieve a four-fold reduction in the number of algebraic equations, approximating the integral equation. For  $m < 1$ , the tip is smooth, and we took  $\varepsilon = 0$ . For  $m > 1$  there is a cusp at  $x = -\Lambda$  that our numerical method can not handle. A similar difficulty arises for  $m = 1$  if the wedge angle is very small. A positive  $\varepsilon$  allows one to employ the method, if the node spacing in the cutoff region is less than  $\varepsilon^m$ .

We measured the retreat distance of the tip  $L(t)$  and the interface shape at different times for three values of  $m$ :  $m = 1/4$ ,  $1/2$  and  $5/4$ , and also for three different wedge angles for  $m = 1$ . In the process of relaxation, each of these domains ultimately becomes a perfect circle. Therefore, to observe the self-similar asymptotics we performed the measurements at times much shorter than the characteristic time of relaxation toward a circle. In addition, to minimize the influence of other tips, we performed the measurements sufficiently close to a chosen tip (at distances much smaller than the distance between the chosen tip and the neighboring tip). These two limitations are especially relevant at  $m < 1$ , where theory predicts self-similarity at sufficiently long times. On the contrary, at  $m > 1$  we performed the measurements at very short times. Here the main limitation comes from the presence of the cutoff, which necessitates a sufficiently long “waiting time” so that the influence of the cutoff on the solution can be neglected.

For  $m = 1/4$  we took  $\Lambda = 2 \times 10^4$  and the minimum node spacing  $\delta S = 1/2$ . The spacing increased exponentially with the distance from the tip, and the initial number of nodes was  $2 \times 10^3$  (here and in the following – per quarter of the interface). For  $m = 1/2$  we chose  $\Lambda = 10^5$ ,  $\delta S = 1$  and the initial number of nodes  $10^3$ . The set of numerical parameters for  $m = 5/4$  was  $\Lambda = 10^{-3}$ ,  $\delta S = 10^{-8}$ ,  $\varepsilon = (2 \times 10^{-8})^{4/5} = 6.93 \times 10^{-7}$ , and the initial number of nodes 1200.

For  $m = 1$  and the wedge angles  $\theta = 10^\circ$  and  $5^\circ$  we used  $\Lambda = 1$ ,  $\delta S = 10^{-5}$ , and the initial number of nodes  $10^3$ . The cutoff parameter  $\varepsilon$  was chosen to be  $\varepsilon = 3\delta S \cot \theta \approx 0.017$  for  $\theta = 10^\circ$ , and  $0.034$  for  $\theta = 5^\circ$ . For  $\theta = 2^\circ$  we took  $\Lambda = 3 \cdot 10^{-3}$ ,  $\delta S = 10^{-6}$ , the initial number of nodes  $2 \cdot 10^3$ , and the cutoff parameter  $\varepsilon \approx 2.8 \cdot 10^{-5}$ .

In all cases the time step was chosen to be  $10^{-3}$  times the maximum of the ratio of the interface curvature radius and the interface speed at the same node. This choice of numerical parameters was dictated by the fact that, at  $0 < m < 1$ , we were interested in a long-time behavior, whereas at  $m > 1$  we needed to focus on very earlier times, in order to observe the predicted self-similarity and scalings.

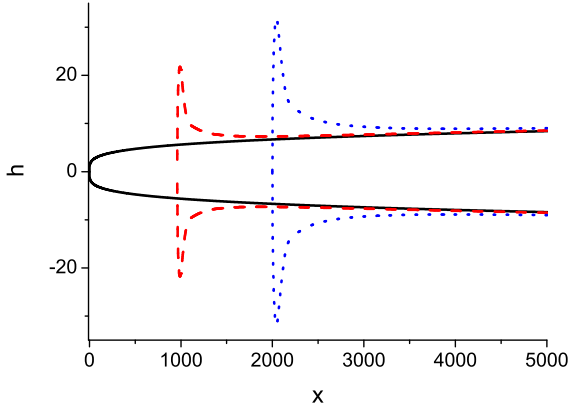


Fig. 2. Snapshots of a part of the simulated system for  $m = 1/4$  at times  $t = 0$  (the black solid line),  $2.7 \times 10^5$  (the red dashed line) and  $1.2 \times 10^6$  (the blue dotted line). Notice the large difference between the horizontal and vertical scales.

### 3.2. Numerical results

Figure 2 shows snapshots of a part of the system for  $m = 1/4$  at times  $t = 0$ ,  $2.7 \times 10^5$  and  $1.2 \times 10^6$ . One can see a lobe developing and growing with time. Shown in Fig. 3a is the retreat distance  $L(t)$  versus time. A power law fit yields exponent  $0.50$  which coincides with the predicted theoretical value  $1/2$ , see Eq. (16). It is more convenient numerically to measure the local maximum height of the interface  $h^{max}(t)$ , rather than the curvature radius at the tip  $R(t)$ . Because of the self-similarity, the quantities  $h^{max}(t)$  and  $R(t)$  are expected to exhibit the same power law dependence (of course, with different pre-factors). Fig. 3b shows  $h^{max}$  versus time in the case of  $m = 1/4$ . It is seen that this dependence approaches a power law. The fitted exponent

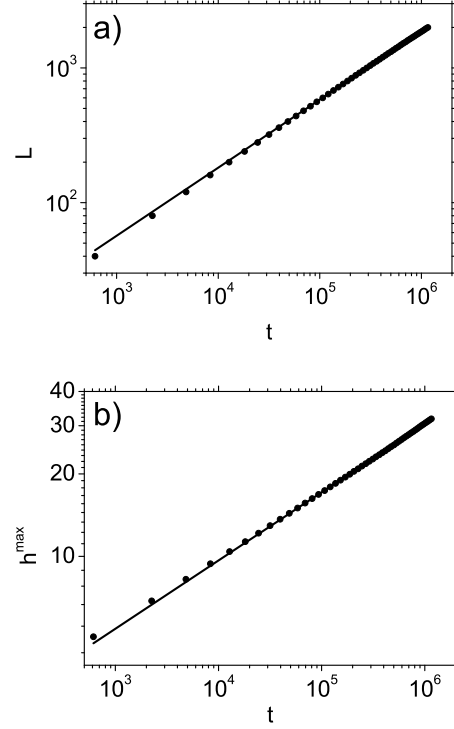


Fig. 3. Figure a shows, in a log-log scale, the retreat distance  $L(t)$  and its power-law fit  $1.73 t^{0.50}$  for the case of  $m = 1/4$ . Figure b shows, in a log-log scale, the local maximum interface elevation,  $h^{max}(t)$ , and its power-law fit  $0.97 t^{0.25}$ .

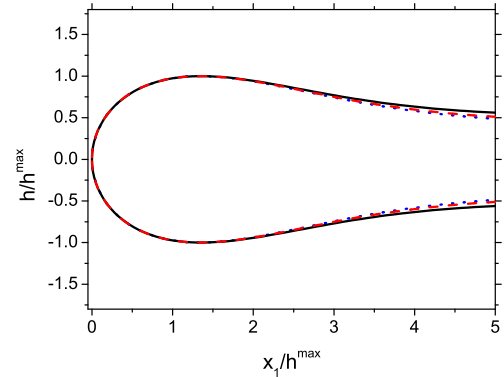


Fig. 4. Self-similarity at  $m = 1/4$ . Shown is the shape function  $h(x_1, t)$ , rescaled to the local maximum elevation  $h^{max}$ , versus the coordinate  $x_1$ , rescaled to  $h^{max}$ , at times  $t = 8.35 \times 10^3$  (the black solid line),  $1.07 \times 10^5$  (the red dashed line) and  $1.16 \times 10^6$  (the blue dotted line).

is  $0.25$ , in excellent agreement with the theoretical value  $1/4$ . Figure 4 demonstrates the presence of a self-similar region in the shape function for  $m = 1/4$ . Also noticeable is a rapid (in time) convergence to the self-similar shape in the lobe region, and a slower convergence in the neck (the neck can be identified

with region II of our theory, as in Ref. [12]).

The numerical results for  $m = 1/2$  are presented in Figures 5, 6 and 7. Here too power laws for  $L(t)$  and  $R(t)$  are observed, and the fitted exponents 0.44 and 0.28 are in good agreement with theoretical values  $3/7 \simeq 0.43$  and  $2/7 \simeq 0.29$ , respectively. The shape function again shows self-similarity, with a rapid (in time) convergence in the lobe region, and a much slower convergence in the neck.

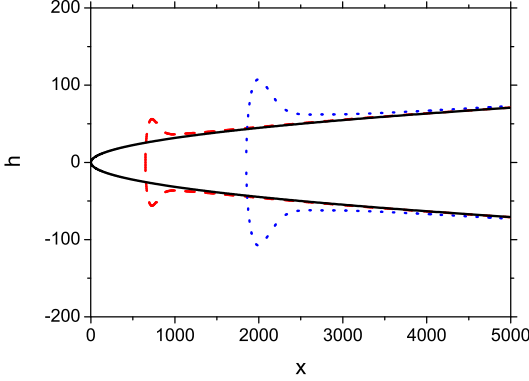


Fig. 5. Snapshots of a part of the simulated system for  $m = 1/2$  at times  $t = 0$  (the black solid line),  $1.01 \times 10^6$  (the red dashed line) and  $1.1 \times 10^7$  (the blue dotted line). Notice the large difference between the horizontal and vertical scales.

The numerical results for  $m = 5/4$  are shown in Figures 8, 9 and 10. Here the self-similar regime is observed at very short times. The observed exponents of the power laws (0.29 for  $\alpha$  and 0.35 for  $\beta$ ) are in good agreement with theoretical values  $\alpha = 0.3$  and  $\beta = 0.35$ . The shape function shows self-similarity in the lobe region, and a rapid deterioration of self-similarity in the neck as the time increases.

Our numerical results for the dynamic exponents  $\alpha$  and  $\beta$  at different  $m$  are summarized in Fig. 11. It can be seen that they follow theoretical curves predicted by Eq. (16). The numerically found coefficients  $a$  and  $b$  of the power laws are presented in Fig. 12.

Figure 13 depicts, on a single plot, a set of rescaled shape functions for four different values of  $m$ . Three of them: for  $m = 1/4$ ,  $1/2$  and  $5/4$ , were computed in the present work, they are the same as shown in Figures 4, 7 and 10, respectively. The shape function for  $m = 0$  is taken from Ref. [12]. Remarkably, all the shape functions coincide in the lobe region. That is, although the retreat distance and the local maximum elevation of the interface depend on  $m$ , the rescaled interface shape is independent of  $m$ , as

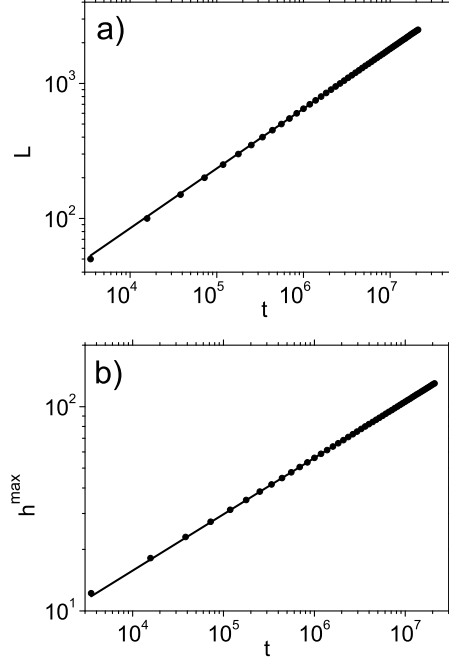


Fig. 6. Figure a shows, in a log-log scale, the retreat distance  $L(t)$  and its power-law fit  $1.43 t^{0.44}$  for the case of  $m = 1/2$ . Figure b shows, in a log-log scale, the local maximum interface elevation,  $h^{max}(t)$ , and its power-law fit  $1.24 t^{0.28}$ .

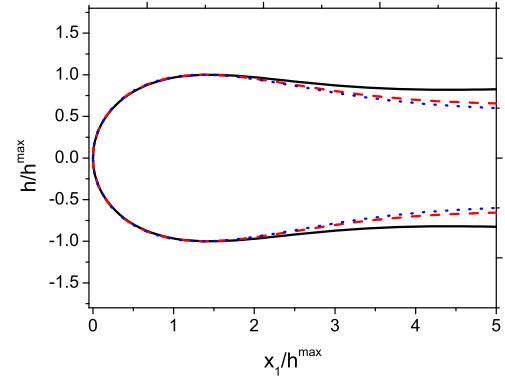


Fig. 7. Self-similarity at  $m = 1/2$ . Shown is the shape function  $h(x_1, t)$ , rescaled to the local maximum elevation  $h^{max}$ , versus the coordinate  $x_1$ , rescaled to  $h^{max}$ , at times  $t = 1.57 \times 10^4$  (the black solid line),  $10^6$  (the red dashed line) and  $1.06 \times 10^7$  (the blue dotted line).

long as  $m \neq 1$ . Figure 13 shows it very clearly in the lobe region. We believe, however, that the rescaled shape functions actually coincide in the neck too, and that the self-similar shape function computed for  $m = 0$  in Ref. [12] (see Fig. 13) is valid for *any*  $m \neq 1$ . Unfortunately, it is hard to prove this conjecture numerically. We observed that, at  $m < 1$ , non-self-similar corrections to the self-similar solu-

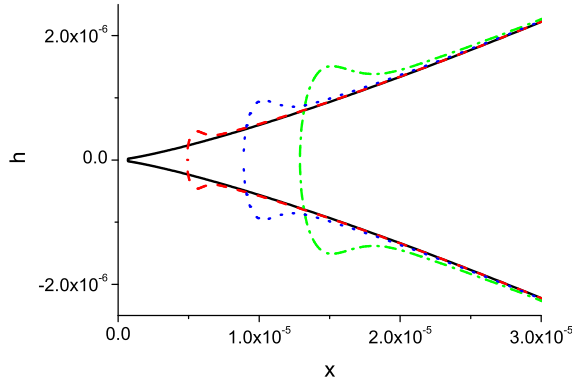


Fig. 8. Snapshots of a part of the simulated system for  $m = 5/4$  at times  $t = 0$  (the black solid line),  $3.2 \times 10^{-19}$  (the red dashed line),  $2.5 \times 10^{-18}$  (the blue dotted line), and  $8.7 \times 10^{-18}$  (the green dash-dotted line). Notice the large difference between the horizontal and vertical scales.

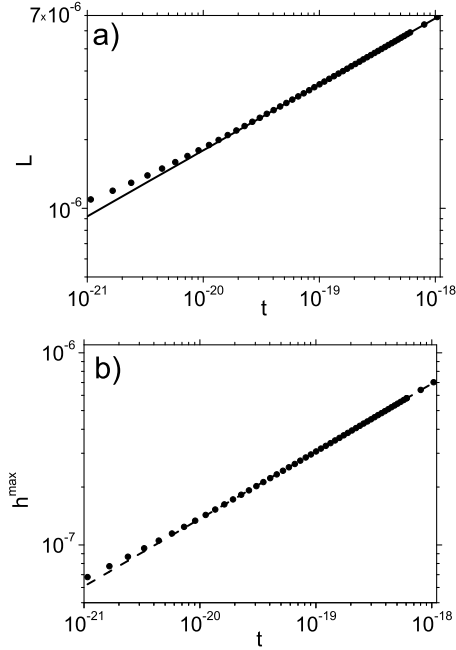


Fig. 9. Figure a shows, in a log-log scale, the retreat distance  $L(t)$  and its power-law fit  $1.1t^{0.29}$  for the case of  $m = 5/4$ . Figure b shows, also in a log-log-scale, the local maximum elevation  $h^{max}(t)$  (the circles) and its power-law fit  $1.6t^{0.35}$ .

tion in the neck region decay very slowly with time when  $m$  is close to 1. As a result, one should go to prohibitively long times (and prohibitively large numerical domain sizes) in order to reach the “pure” similarity regime in the neck. In its turn, at  $m > 1$  corrections to the self-similar solution grow very fast with time when  $m$  is close to 1, so one has to go to prohibitively small times in order to observe the “pure” self-similarity in the neck. This is hard to

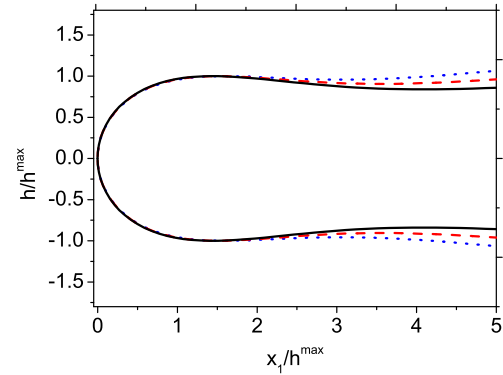


Fig. 10. Self-similarity at  $m = 5/4$ . Shown is the shape function  $h(x_1, t)$ , rescaled to the local maximum elevation  $h^{max}$ , versus the coordinate  $x_1$ , rescaled to  $h^{max}$ , at times  $t = 1.1 \times 10^{-19}$  (the black solid line),  $4.9 \times 10^{-18}$  (the red dashed line), and  $1.1 \times 10^{-16}$  (the blue dotted line).

achieve in view of the presence of the numerical cut-off at  $m > 1$ , which requires sufficiently *long* waiting times before its influence on the scaling results becomes small.

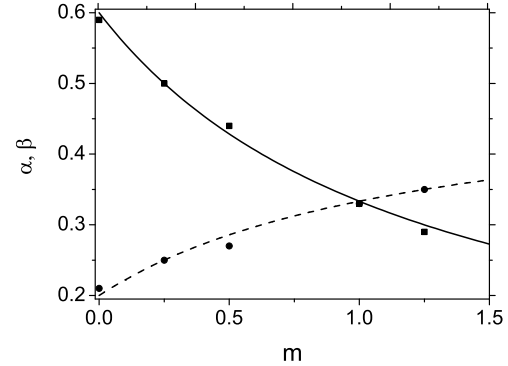


Fig. 11. The exponents  $\alpha$  and  $\beta$  of the power laws (8) versus the parameter  $m$ . The solid and dashed lines show theoretical predictions [see Eq. (16)] for  $\alpha$  and  $\beta$ , respectively. The corresponding numerical results are shown by the squares and circles, respectively. The numerical values of  $\alpha$  and  $\beta$  for  $m = 1/4$ ,  $1/2$  and  $5/4$  are computed in this work, while those for  $m = 0$  and  $m = 1$  are taken from Refs. [12] and [13], respectively.

Is there any connection between the universal scaled shape shown in Fig. 13 and the rescaled interface shapes of the wedge ( $m = 1$ ) which depend on the wedge angle? To address this question, we simulated the relaxation dynamics of several wedges with small angles. Figure 14 shows self-similar shape functions for three different values of the wedge angle:  $10^\circ$ ,  $5^\circ$  and  $2^\circ$ . Shown on the same graph is the shape function for  $m = 0$ . Remarkably, all the shape functions coincide in the lobe region.



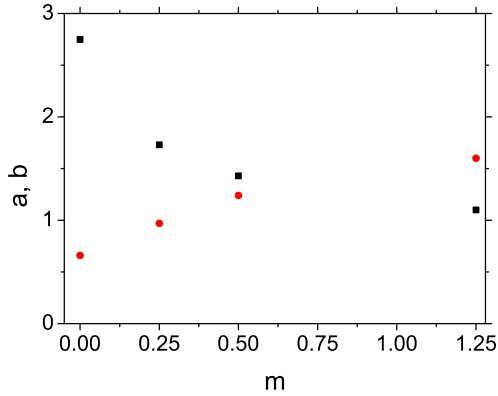


Fig. 12. The numerically found coefficients  $a$  (squares) and  $b$  (circles) of the power laws (8) versus the parameter  $m$ . The values for  $m = 1/4$ ,  $1/2$  and  $5/4$  are computed in this work, while those for  $m = 0$  are taken from Ref. [12].

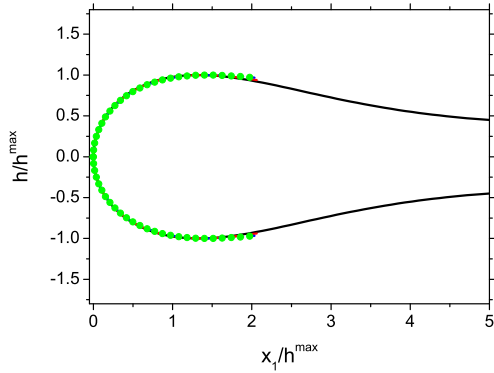


Fig. 13. Self-similar shape functions at four different values of  $m$ :  $m = 0$  (the black solid line),  $1/4$  (the red dashed line),  $1/2$  (the blue dotted line) and  $5/4$  (the green symbols).

Furthermore, the numerics strongly suggests that, as the wedge angle tends to zero, the shape function approaches that for  $m = 0$  *everywhere*. That is, the observed universal shape function for  $m \neq 1$  coincides with the shape function obtained in the zero-angle limit for  $m = 1$ .

#### 4. Summary

We have investigated the dynamics of relaxation, by surface tension, of a family of curved interfaces, dividing an inviscid and viscous fluids in a Hele-Shaw cell, and characterizable by a single exponent  $m$ . A stripe  $m = 0$ , a wedge  $m = 1$  and a generic cusp  $m = 2$  that appears after a pinch-off event, represent particular cases of these more general shapes. Combining simple analytic arguments with a robust numerical method, we have found that, for any  $m \neq 1$ , the relaxation dynamics of the interfaces ex-

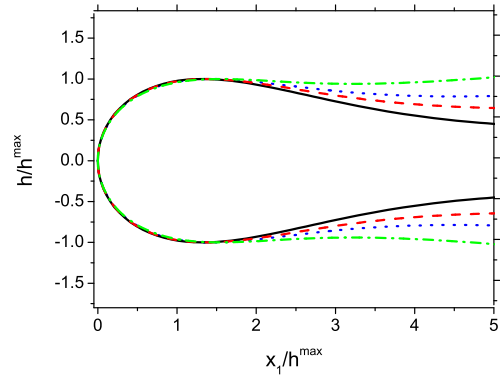


Fig. 14. Self-similar shape functions for  $m = 1$  at three different values of the wedge angle:  $10^\circ$  (the green dash-dotted line),  $5^\circ$  (the blue dotted line), and  $2^\circ$  (the red dashed line). The black solid line shows the shape function for  $m = 0$ .

hibit self-similar intermediate asymptotics: a late-time asymptotics for  $0 \leq m < 1$  and an early-time asymptotics for  $m > 1$ . Our theoretical predictions for the dynamic exponents of the retreat distance and the local maximum elevation of the interface versus time, at different  $m$ , are in excellent agreement with numerical simulations. We have found that, for  $m \neq 1$ , the rescaled interface shape is universal, that is, it does not depend on  $m$  in the similarity region. Remarkably, the same rescaled interface shape also emerges in the case of  $m = 1$  (where the self-similarity is exact and holds for the whole interface at all times  $t > 0$ ), in the limit of zero wedge angle.

Future work should provide a more complete theory that would explain the surprising findings presented here. We hope that this work (see also Refs. [12,13]) will facilitate experimental and further theoretical efforts aimed at a better understanding of the “simple” unforced Hele-Shaw flow.

#### Acknowledgment

We thank Omri Gat for a useful discussion. This work was supported by the Israel Science Foundation (Grant No. 107/05), by the German-Israeli Foundation for Scientific Research and Development (Grant I-795-166.10/2003), and by the Russian Foundation for Basic Research (Grant No. 05-01-000964).

## References

- [1] E. Sharon, M.G. Moore, W.D. McCormick, and H.L. Swinney, Phys. Rev. Lett. **91** (2003) 205504.
- [2] P.G. Saffman and G.I. Taylor, Proc. R. Soc. London, Ser. A **245** (1958) 312.
- [3] L. Paterson, J. Fluid Mech. **113** (1981) 513.
- [4] J.S. Langer, in *Chance and Matter*, edited by J. Souletie, J. Vannimenus, and R. Stora, Elsevier, Amsterdam, 1987.
- [5] D. Bensimon, L.P. Kadanoff, S. Liang, B.I. Shraiman, and C. Tang, Rev. Mod. Phys. **58** (1986) 977.
- [6] D.A. Kessler, J. Koplik, and H. Levine, Adv. Physics **37** (1988) 255.
- [7] J. Casademunt and F.X. Magdaleno, Phys. Rep. **337** (2000) 1.
- [8] P. Constantin and M. Pugh, Nonlinearity **6** (1993) 393.
- [9] R. Almgren, Phys. Fluids **8** (1996) 344.
- [10] M. Conti, A. Lipshtat, and B. Meerson, Phys. Rev. E **69** (2004) 031406.
- [11] The damping rates of small sinusoidal perturbations of flat and circular interfaces are given by the zero-flow-rate limit of Eq. (10) of Ref. [2] (flat interface), and of Eq. (11) of Ref. [3] (circular interface).
- [12] A. Vilenkin, B. Meerson, and P.V. Sasorov, Phys. Rev. Lett. **96** (2006) 044504.
- [13] O. Gat, B. Meerson, and A. Vilenkin, Phys. Rev. E **73** (2006) 065302(R).
- [14] J.D. Jackson, Classical Electrodynamics, Wiley, New York, 1975, p. 76.
- [15] J.C. de Munck, IEEE Trans. Biomed. Eng. **39** (1992) 986.
- [16] A. Vilenkin and B. Meerson, arXiv physics/0512043.
- [17] A. Greenbaum, L. Greengard, and G.B. McFadden, J. Comput. Phys. **105** (1993) 267.